Research in Astron. Astrophys. **2010** Vol. **10** No. **10**, 1005–1012
http://www.raa-journal.org *http://www.iop.org/journals/raa*

***R**esearch in*
***A**stronomy and*
***A**strophysics*

Biases in hydrostatic mass profiles introduced by hot gas substructures: *Chandra* study of four galaxy clusters*

Li-Yi Gu, Yu Wang, Jun-Hua Gu, Jing-Ying Wang, Zhen-Zhen Qin, Meng-Yu Yao, Jian-Long Yang and Hai-Guang Xu

Department of Physics, Shanghai Jiao Tong University, Shanghai 200240, China;
alfred_gly@sjtu.edu.cn

Received 2010 April 2; accepted 2010 May 27

Abstract By analyzing the azimuthal variations of total gravitating mass profiles in the central $300\,h_{71}^{-1}$ kpc regions of four galaxy clusters with *Chandra* data, we find that the azimuthally-averaged mass profiles may have been systematically underestimated by 16^{+9}_{-8}% at 1σ significance in the 50–100 h_{71}^{-1} kpc regions, probably due to the prevailing existence of 2-D hot gas substructures in 100–300 h_{71}^{-1} kpc. The mass biases become negligible (-7^{+11}_{-9}%) at $> 150\,h_{71}^{-1}$ kpc. We confirm the results that the gas temperature maps can be used to probe the departure from hydrostatic equilibrium and help quantify the systematic biases in X-ray mass measurements in the central regions of clusters.

Key words: cosmology: dark matter — galaxies: clusters: general — galaxies: intergalactic medium — X-rays: galaxies: clusters

1 INTRODUCTION

The gravitating mass distribution in galaxy clusters is a sensitive test of the properties of dark matter (e.g., Clowe et al. 2004; Markevitch et al. 2004; Sand et al. 2008). Since the intracluster medium (ICM) in relaxed galaxy clusters is expected to be in hydrostatic equilibrium on the scale of clusters (Sarazin 1988), the X-ray emission of ICM can be used to constrain the mass distributions of relaxed galaxy clusters. Recent X-ray observations with high-quality *Chandra*, *XMM-Newton*, and *Suzaku* data provide precise measurements of mass distributions with uncertainties below 15% up to r_{500} (e.g., Vikhlinin et al. 2006).

In order to assess the reliability of the X-ray mass estimate, much effort has been devoted to comparing it with the results obtained from gravitational lensing analysis, which does not require the hydrostatic equilibrium assumption (e.g., Wu & Fang 1996; Squires et al. 1996; Allen 1998). As shown in a range of recent work (e.g., Mahdavi et al. 2008; Zhang et al. 2008, 2010; Vikhlinin et al. 2009), cluster masses calculated with weak lensing analysis are systematically larger than those obtained in X-ray by ≈ 10% at r_{500}; the discrepancies become nearly negligible within 5% at r_{2500} ($\approx 0.4\,r_{500}$). Hence, the hydrostatic mass estimate is fairly accurate on 0.4–1.0 r_{500} scales. For inner regions within $\sim 0.2\,r_{500}$, however, such a systematic comparison between X-ray and weak lensing masses is lacking. Previous X-ray and numerical studies suggested that the hydrostatic equilibrium

* Supported by the National Natural Science Foundation of China.

assumption may not stand in the central regions of a cluster. For example, Markevitch et al. (2001) showed that the hydrostatic mass measured at $80\,h_{71}^{-1}$ kpc ($\approx 0.1\,r_{500}$) south of the cluster center of A1795 is biased towards low by a factor of two due to the gas bulk motion caused by subcluster infall. In addition, as shown in recent numerical simulations, the X-ray mass measurements in the central $0.2\,r_{500}$ are possibly biased by $\approx$ 20%–30% due to ICM substructures created by minor merging events (e.g., Nagai et al. 2007) and/or activity of active galactic nuclei (AGNs; e.g., Guo & Mathews 2010). Hence, substructure studies pose an important constraint on the validity of the hydrostatic equilibrium assumption in the central regions of clusters.

The 2-D gas temperature map is an important tool for detecting such ICM substructures (e.g., Andersson et al. 2009). In a recent work, Zhang et al. (2009) calculated the gas temperature maps of four galaxy clusters with the *XMM-Newton* data, and detected apparent temperature substructures with $\Delta T \approx 0.5 - 2.0$ keV at $\gtrsim 0.2\,r_{500}$ ($\approx 300\,h_{71}^{-1}$ kpc) that significantly show hydrostatic masses that deviate from values expected from $M - Y_{\rm X}$ and $M - M_{\rm gas}$ relations. By analyzing the gas temperature maps of nine relaxed galaxy clusters created with *Chandra* data, Gu et al. (2009; hereafter G09) reported the existence of prevailing 2-D hot gas substructures with $\Delta T \approx 2.0 - 3.0$ keV on $\sim 100\,h_{71}^{-1}$ kpc scales in 0.1–0.2 r_{500} ($\approx$ 100–300 h_{71}^{-1} kpc) regions, and speculatively ascribed the hot substructures to be remnants of buoyant bubbles, into which the central AGN has injected energy via shocks and turbulence (see McNamara & Nulsen 2007 for a review). By calculating the thermal conduction timescales of these substructures, G09 pointed out that the detected hot gas substructures are formed within $\approx 2 \times 10^8$ yr (see table 4 of G09), comparable to the sound crossing timescale ($\approx 10^8$ yr), which indicates that the substructures are probably not in hydrostatic equilibrium. So far, it is unclear to what extent such hot gas substructures cause the X-ray measurements of gravitating mass profiles to deviate in the central regions of clusters.

In this work, we revisit the *Chandra* data of four galaxy clusters refined from the G09 sample. By analyzing azimuthal variations of hydrostatic mass profiles, we examine quantitatively the amplitudes and extents of possible biases in azimuthally-averaged mass profiles due to the 2-D hot gas substructures detected in G09. Throughout the paper, we assume $H_0 = 71 h_{71}$ km s^{-1} Mpc^{-1}, a flat universe for which $\Omega_M = 0.27$ and $\Omega_\Lambda = 0.73$, adopt the solar abundance standards of Grevesse & Sauval (1998), and quote errors according to the 68% confidence level unless stated otherwise.

2 SAMPLE AND DATA PREPARATION

Our sample is comprised of four relaxed galaxy clusters, A1068, A1650, A2244, and A2556 (Table 1), drawn from the flux-limited ($F_{\rm X,0.7-8.0\,keV} > 5.0 \times 10^{-12}$ erg s^{-1} cm^{-2}), intermediate-redshift ($z \simeq 0.1$) galaxy cluster sample presented in G09. The four clusters are suited to our purpose, since (1) the high-quality *Chandra* data of the four clusters allow us to measure deprojected temperature profiles with uncertainties $\lesssim 0.5$ keV at the 90% confidence level (see fig. 3a of G09) and (2) the azimuthal distributions of hot substructures in the four clusters allow us to define substructure-free sectors (see Sect. 3) with span angles $> 150°$, which are used as references to examine the possible biases in azimuthally-averaged mass profiles (Sect. 5). By applying the latest CIAO 4.2 and CALDB 4.2.0, we reprocessed all the *Chandra* data following the data reduction pipeline described in G09. We utilized the *Chandra* blank-sky template for the S3 CCD as the background in the subsequent spectral analysis.

3 SECTOR SELECTION

In order to quantitatively determine the possible biases in hydrostatic mass profiles due to 2-D hot gas substructures detected in G09, we calculate and compare three types of total gravitating mass profiles for each cluster, including the azimuthally-averaged profiles (hereafter Type-A profiles), profiles for sectors containing the 2-D hot gas substructures (hereafter Type-H profiles), and profiles for counterpart sectors where no apparent hot gas substructure is detected (hereafter Type-C profiles).

Table 1 Basic Properties and Best-fit Temperature Models of Sample Clusters

Name (Type)	Redshift	kT^a (keV)	$R_{\rm out}{}^b$ (h_{71}^{-1} kpc)	$T_0{}^c$ (keV)	$T_1{}^c$ (keV)	$R_{\rm c}{}^c$ (h_{71}^{-1} kpc)	η^c	dT/dR^d (keV/h_{71}^{-1} kpc)
A1068 (Type-A)	0.1375	$3.6^{+0.1}_{-0.1}$	530 ± 110	$2.7^{+0.1}_{-0.1}$	$8.5^{+0.3}_{-0.3}$	96^{+8}_{-7}	$1.9^{+0.1}_{-0.1}$	$0.033^{+0.001}_{-0.002}$
A1068 (Type-H)			530 ± 110	$2.9^{+0.1}_{-0.1}$	$2.7^{+0.5}_{-0.3}$	$[96^{+8}_{-7}]$	$3.9^{+0.6}_{-0.8}$	$0.048^{+0.005}_{-0.002}$
A1068 (Type-C)			530 ± 110	$1.0^{+0.3}_{-0.2}$	$6.3^{+0.5}_{-0.5}$	$[96^{+8}_{-7}]$	$0.3^{+0.1}_{-0.1}$	$0.014^{+0.003}_{-0.003}$
A1650 (Type-A)	0.0845	$6.0^{+0.2}_{-0.3}$	460 ± 80	$2.6^{+0.3}_{-0.3}$	$7.2^{+1.0}_{-0.6}$	103^{+10}_{-6}	$0.4^{+0.1}_{-0.1}$	$0.018^{+0.004}_{-0.004}$
A1650 (Type-H)			460 ± 80	$3.0^{+0.2}_{-0.1}$	$6.4^{+0.3}_{-0.3}$	$[103^{+10}_{-6}]$	$1.9^{+0.1}_{-0.3}$	$0.042^{+0.005}_{-0.003}$
A1650 (Type-C)			460 ± 80	$2.9^{+0.1}_{-0.2}$	$5.6^{+0.6}_{-0.5}$	$[103^{+10}_{-6}]$	$0.2^{+0.1}_{-0.1}$	$0.004^{+0.003}_{-0.002}$
A2244 (Type-A)	0.0968	$5.3^{+0.1}_{-0.1}$	390 ± 90	$3.0^{+0.7}_{-0.6}$	$5.7^{+0.5}_{-0.4}$	85^{+15}_{-13}	$0.3^{+0.1}_{-0.1}$	$0.006^{+0.002}_{-0.002}$
A2244 (Type-H)			390 ± 90	$5.0^{+0.2}_{-0.4}$	$3.8^{+0.5}_{-0.3}$	$[85^{+15}_{-13}]$	$2.0^{+0.7}_{-0.5}$	$0.022^{+0.011}_{-0.008}$
A2244 (Type-C)			390 ± 90	$0.2^{+0.1}_{-0.1}$	$10.0^{+0.8}_{-0.9}$	$[85^{+15}_{-13}]$	$0.1^{+0.1}_{-0.1}$	$-0.001^{+0.003}_{-0.002}$
A2556 (Type-A)	0.0871	$3.2^{+0.1}_{-0.1}$	380 ± 80	$2.9^{+0.3}_{-0.1}$	$2.0^{+0.2}_{-0.2}$	62^{+7}_{-8}	$3.0^{+0.5}_{-0.7}$	$0.014^{+0.006}_{-0.003}$
A2556 (Type-H)			380 ± 80	$2.7^{+0.2}_{-0.1}$	$3.1^{+0.5}_{-0.4}$	$[62^{+7}_{-8}]$	$2.5^{+1.1}_{-0.8}$	$0.027^{+0.009}_{-0.006}$
A2556 (Type-C)			380 ± 80	$3.2^{+0.2}_{-0.2}$	$6.7^{+0.3}_{-0.2}$	$[62^{+7}_{-8}]$	$1.1^{+0.1}_{-0.2}$	$0.003^{+0.002}_{-0.005}$

[a] Average gas temperatures in central $400\,h_{71}^{-1}$ kpc regions.
[b] Mean radii of the outermost bins used to calculate deprojected temperature profiles. Errors give widths of the bins.
[c] Best-fit parameters of the analytic model for temperature profiles, as defined in Eq. (1). To avoid strong intrinsic degeneracy between parameters, we let $R_{\rm c}$ be the same value among Type-A, Type-H, and Type-C profiles for each cluster, while T_0, T_1, and η are set free.
[d] Average gradients of deprojected temperature profiles in 50–100 h_{71}^{-1} kpc.

To define the Type-H and Type-C sectors accurately, we calculate 2-D temperature maps of the four clusters based on a binning method introduced by Sanders (2006), which creates 2-D bins primarily along the azimuthal direction and thus is suited for determining the azimuthal distributions of hot gas substructures. First we separate the central $300\,h_{71}^{-1}$ kpc regions of each cluster into 20 – 40 bins; each bin contains $\approx$ 5000 counts after the point sources are excluded. Then we calculate the projected temperature for each bin by fitting the extracted spectrum with an absorbed APEC model coded in the `XSPEC` 12.4.0 package. In the fitting, we fix absorption column density $N_{\rm H}$ to the Galactic value (Dickey & Lockman 1990), while leaving the ICM metal abundance free. The typical 1σ temperature error is ~ 0.2 keV for each bin. The obtained temperature maps, as shown in Figure 1, are consistent with the maps presented in G09 within the uncertainty caused by different binning schemes. We find that there exist apparent high temperature regions in 100–200 h_{71}^{-1} kpc, where the gas temperatures are typically higher than that of the environment by $\Delta T_{\rm X} \approx 1 - 3$ keV, nicely consistent with the wavelet detection result reported in G09. By defining hot substructures as temperature excesses > 1 keV over the azimuthally-averaged values, we separate the central regions of the clusters into Type-H and Type-C sectors, which have average span angles of $\approx 160°$ and 200°, respectively (Fig. 1).

4 DEPROJECTED GAS TEMPERATURE AND DENSITY PROFILES

Following the method in G09, we calculate the deprojected gas temperature profiles in the inner $400\,h_{71}^{-1}$ kpc region. The target region is divided into concentric annuli (Type-A) and pie regions (Type-H and C), all centered on the X-ray peak. We fit the extracted spectra with an absorbed APEC model. When the absorption is fixed as above, and employ the PROJCT model to correct the pro-

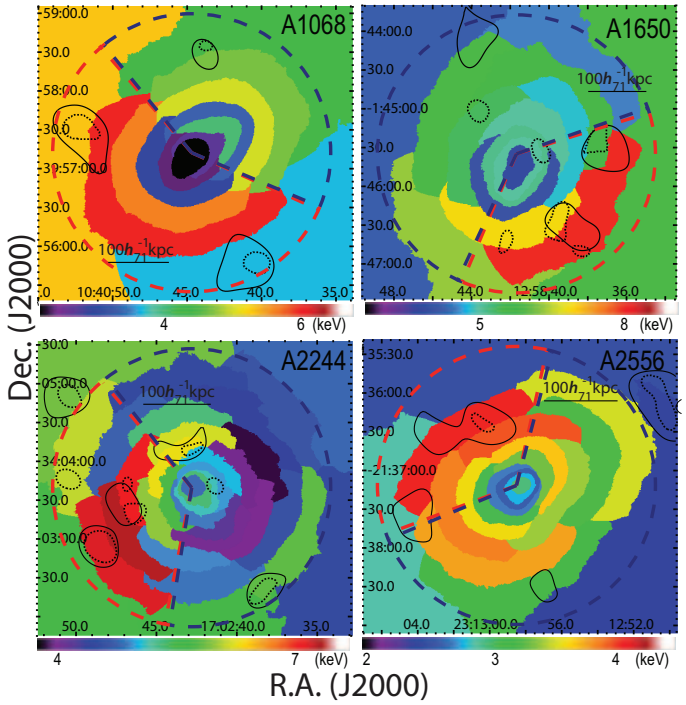

Fig. 1 Projected gas temperature maps of four sample clusters, calculated using the method described in Sect. 3. Based on temperature maps presented in fig. 4 of G09, hot gas substructures detected with a wavelet algorithm on characteristic scales $\approx$ 100–200 h_{71}^{-1} kpc and 50–100 h_{71}^{-1} kpc are marked with solid and dotted contours, respectively (see sect. 3.3.2 of G09 for details). Red and blue dashed lines denote Type-H and Type-C sectors used in our spectral analysis (Sect. 4), respectively.

jection effect. When the metal abundance of an annulus or pie region is poorly constrained, we tie it to that of an adjacent region for better statistics, which is found to slightly affect the temperature profile. To describe the obtained best-fit temperature profiles in a smooth form, we adopt the analytic model introduced in Allen et al. (2001),

$$T(R) = T_0 + T_1 \frac{(R/R_c)^\eta}{1 + (R/R_c)^\eta}. \tag{1}$$

The best-fit parameters (T_0, T_1, R_c, and η) are listed in Table 1, and the obtained smooth Type-A, Type-H, and Type-C temperature profiles ($T_A(R)$, $T_H(R)$, and $T_C(R)$, respectively) are shown in Figure 2. By comparing $T_A(R)$ profiles with $T_C(R)$ profiles, we find that the mean gradients of $T_A(R)$ profiles in 50–100 h_{71}^{-1} kpc are significantly larger than those of $T_C(R)$ profiles, by a factor ≥ 1.8 (the 68% confidence level; Table 1), due to the hot substructures found in the 100–300 h_{71}^{-1} kpc regions (Fig. 1).

In order to achieve a fine spatial resolution for the gas density profiles, we divide each annulus (Type-A) and pie region (Type-H and Type-C) into three parts, with each having 1/3 of the counts in the original region. We fit the extracted spectra with the PROJCT(WABS×APEC) model, when absorption is fixed as above, and gas temperature and metal abundance are determined by linear interpolations of the best-fit deprojected profiles. Following the method described in, e.g., Johnson et al. (2009), we calculate the deprojected gas density profiles from the best-fit model normalizations.

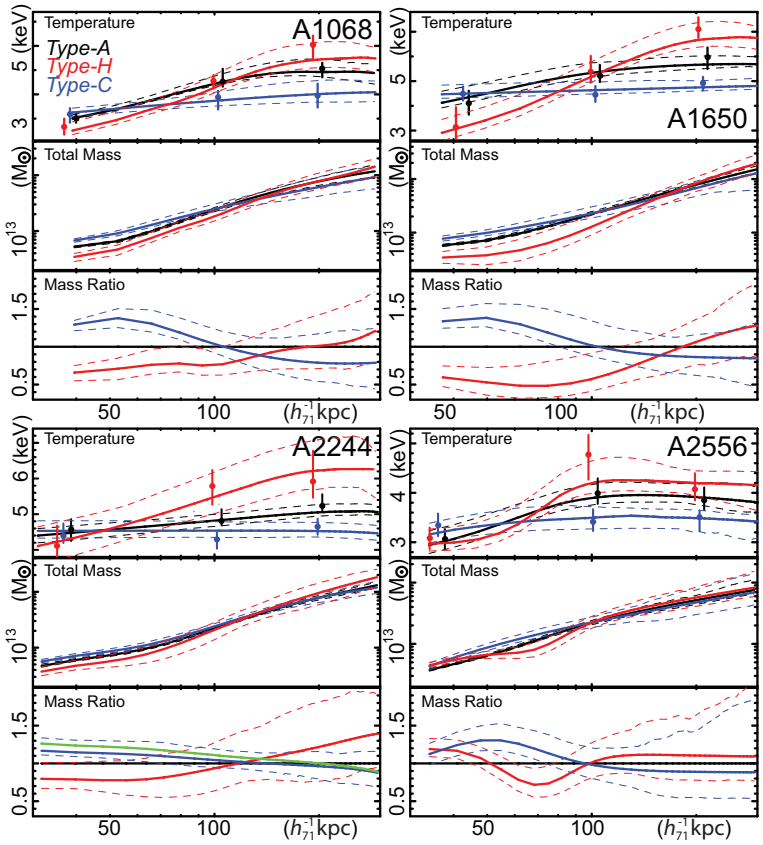

Fig. 2 Deprojected gas temperature (*upper panel*), total gravitating mass (*middle panel*), and mass ratio (*lower panel*) profiles for each cluster. The deprojected temperature and total mass profiles are calculated for Type-A (*black*), Type-H (*red*), and Type-C (*blue*) regions, and the mass ratio profiles are obtained as $M_{\rm H}(R)/M_{\rm A}(R)$ (*red*) and $M_{\rm C}(R)/M_{\rm A}(R)$ (*blue*). Deprojected Type-A, Type-H, and Type-C temperatures measured in the inner parts ($\approx 40\,h_{71}^{-1}$ kpc) and at typical radii of hot substructures ($\approx 100\,h_{71}^{-1}$ kpc and $200\,h_{71}^{-1}$ kpc) are plotted on the temperature profiles, when the data points of different types are slightly offset for clarity. To keep the figure clear, deprojected temperatures measured at other radii are omitted. The green curve shows the mass ratio profile, $M_{\rm C}^{*}(R)/M_{\rm A}(R)$, after excluding the cool gas substructure detected in A2244 (Sect. 5). All errors are given at the 68% confidence level.

By adopting an empirical two-β model defined in, e.g., equation (7) of Wang et al. (2005), we fit the obtained density profiles in a smooth form. We find that for each cluster, the smooth Type-A, Type-H, and Type-C gas density profiles ($n_{\rm A}(R)$, $n_{\rm H}(R)$, and $n_{\rm C}(R)$, respectively) are consistent with each other within the 68% confidence level.

5 POSSIBLE BIASES OF AZIMUTHALLY-AVERAGED MASS PROFILES

Based on the best-fit deprojected gas temperature and density profiles, we calculate the total gravitating mass profiles under the condition of hydrostatic equilibrium as

$$M(R) = -\frac{kTR}{G\mu m_p}\left(\frac{d\log n}{d\log R} + \frac{d\log T}{d\log R}\right), \tag{2}$$

where G is the gravitational constant, $\mu = 0.609$ is the average molecular weight for fully ionized gas, and m_p is the proton mass. For each cluster, we plot the obtained Type-A, Type-H, and Type-C mass profiles ($M_{\rm A}(R)$, $M_{\rm H}(R)$, and $M_{\rm C}(R)$, respectively) in Figure 2, along with the uncertainties calculated by performing 1000 Monte-Carlo simulations that account for the ranges of gas temperature and density profiles allowed by the data. To quantify the discrepancies among the three mass profiles, we divide $M_{\rm H}(R)$ and $M_{\rm C}(R)$ by $M_{\rm A}(R)$, and show the mass ratio profiles in Figure 2. As listed in Table 2, the average ratio of $M_{\rm C}(R)$ to $M_{\rm A}(R)$ in 50–100 h_{71}^{-1} kpc gives $1.16^{+0.06}_{-0.04}$ for the sample. Since neither apparent surface brightness nor hot gas substructure is detected in Type-C sectors, we assume the ICM in Type-C sectors is close to hydrostatic equilibrium. Hence, the azimuthally-averaged mass profiles are likely to be systematically underestimated by 16^{+6}_{-4}% in the region 50–100 h_{71}^{-1} kpc, while the biases become negligible (-7^{+8}_{-5}%; Table 2) in the region 150–300 h_{71}^{-1} kpc. Accordingly, the average gas mass fractions in 50–100 h_{71}^{-1} kpc calculated with Type-A profiles may have been overestimated by 20 ± 10% (Table 2). By applying $n_{\rm C}(R) \simeq n_{\rm A}(R)$ to Equation (2), we deduce that the systematic biases on $M_{\rm A}(R)$ profiles can be primarily ascribed to the prevailing existence of hot gas substructures in 100–300 h_{71}^{-1} kpc (fig. 1; G09), which are believed to steepen the gradients of $T_{\rm A}(R)$ profiles in 50–100 h_{71}^{-1} kpc by a factor > 1.8 (Sect. 4). This result confirms previous findings in, e.g., Finoguenov et al. (2005) and Zhang et al. (2009), showing that the substructure diagnostics based on 2-D temperature maps can be used to probe the departure from hydrostatic equilibrium and help quantify the systematic biases in X-ray mass measurements in the central regions of clusters.

Table 2 Comparison between Type-A and Type-C Mass Profiles

$M_{\rm C}(R)/M_{\rm A}(R)\|_{50-100}$ [a]	$M_{\rm C}(R)/M_{\rm A}(R)\|_{150-300}$ [b]	$f_{\rm gas,A}$ [c]	$f_{\rm gas,C}$ [d]
$1.24^{+0.08}_{-0.07}$	$0.88^{+0.15}_{-0.09}$	0.07 ± 0.01	0.05 ± 0.01
$1.15^{+0.11}_{-0.07}$	$0.92^{+0.10}_{-0.10}$	0.07 ± 0.02	0.06 ± 0.02
$1.09^{+0.07}_{-0.06}$	$0.96^{+0.05}_{-0.04}$	0.05 ± 0.01	0.04 ± 0.01
$1.14^{+0.08}_{-0.05}$	$0.95^{+0.09}_{-0.06}$	0.04 ± 0.01	0.04 ± 0.01

[a] Average ratios of $M_{\rm C}(R)$ to $M_{\rm A}(R)$ in 50–100 h_{71}^{-1} kpc regions (Sect. 5).
[b] Average ratios of $M_{\rm C}(R)$ to $M_{\rm A}(R)$ in 150–300 h_{71}^{-1} kpc regions (Sect. 5).
[c] Average gas mass fractions in 50–100 h_{71}^{-1} kpc calculated with Type-A profiles.
[d] Average gas mass fractions in 50–100 h_{71}^{-1} kpc calculated with Type-C profiles.

Next we examine the possibility of other uncertainties involved in the mass measurements. As shown in Figure 1, there exists an apparent cool gas substructure in 50–120 h_{71}^{-1} kpc along the Type-C sector of A2244, with an average temperature 1.2 ± 0.2 keV lower than its ambient ICM. Such off-center cool gas substructures can be ascribed to either minor mergers (e.g., Machacek et al. 2005) or AGN-induced cool gas outflows (e.g., Nulsen et al. 2002). To examine possible deviation of mass profile measurements due to the cool gas substructure, we calculate a corrected Type-C temperature profile $T^*_{\rm C}(R)$ by omitting the deprojected temperatures measured in 50–120 h_{71}^{-1} kpc from the model fitting with Equation (1), and derive corrected mass profile $M^*_{\rm C}(R)$ by applying $T^*_{\rm C}(R)$ to Equation (2). As shown in Figure 2, the obtained $M^*_{\rm C}(R)$ is consistent with $M_{\rm C}(R)$ at the 68% confidence level, while the former appears higher by ≈ 5% on average in 50–120 h_{71}^{-1} kpc. Hence, to account for uncertainty caused by such off-center cool substructures that possibly exist in the central 300 h_{71}^{-1} kpc region, we include an additional 5% error in the total uncertainty budget of the mass profiles.

Another concern is the uncertainty caused by the choice of cluster center. Indeed, as shown in a sample study of Shan et al. (2010), there may exist offsets, up to 36 h_{71}^{-1} kpc, between the lensing center and X-ray peak for relaxed clusters. To assess the induced uncertainty on mass measurements, we assign the center of Type-A and Type-C regions to a random point in the central 36 h_{71}^{-1} kpc

region, and perform deprojected spectral analysis to calculate modified Type-A and Type-C mass profiles ($M_{\rm A}^{**}(R)$ and $M_{\rm C}^{**}(R)$, respectively). By repeating this process ten times for each cluster and comparing the obtained mass ratios $M_{\rm C}^{**}(R)/M_{\rm A}^{**}(R)$ with the original ones, we have estimated a 1σ scatter of 5% in 50–300 h_{71}^{-1} kpc, due to the possible shifts between X-ray and mass centers. This scatter, combined in quadrature with all the uncertainties estimated above, gives 1σ ranges of the mass biases as 16^{+9}_{-8}% and -7^{+11}_{-9}%, in the 50–100 h_{71}^{-1} kpc and 150–300 h_{71}^{-1} kpc regions, respectively.

In addition to uncertainties discussed above, in fact, the X-ray mass profiles may have deviated due to, e.g., off-center dark matter substructures (e.g., Riemer-Sørensen et al. 2009) and additional pressure supports from gas turbulent motions, cosmic rays, and cluster magnetic fields (e.g., Schuecker et al. 2004; Churazov et al. 2008). Due to the lack of weak lensing studies for the four nearby clusters in our sample, it is difficult, for the time beings, to address the possible deviations in hydrostatic mass estimates contributed by these effects.

6 SUMMARY

Using high-quality *Chandra* data of four galaxy clusters, we find that the azimuthally-averaged mass profiles may have been systematically underestimated by 16^{+9}_{-8}% at 1σ significance in 50–100 h_{71}^{-1} kpc, probably due to the prevailing existence of 2-D hot gas substructures in 100–300 h_{71}^{-1} kpc regions. Our result confirms the recent findings in, e.g., Finoguenov et al. (2005) and Zhang et al. (2009), showing that the gas temperature maps can be used to constrain the level of departure from hydrostatic equilibrium in the central regions of clusters.

Acknowledgements We thank the *Chandra* team for making data available via the High Energy Astrophysics Science Archive Research Center (HEASARC). This work was supported by National Natural Science Foundation of China (Grant Nos. 10673008, 10878001 and 10973010), the Ministry of Science and Technology of China (Grant No. 2009CB824900/2009CB24904), and the Ministry of Education of China (the NCET Program).

References

Allen, S. W. 1998, MNRAS, 296, 392
Allen, S. W., Schmidt, R. W., & Fabian, A. C. 2001, MNRAS, 328, L37
Andersson, K., Peterson, J. R., Madejski, G., & Goobar, A. 2009, ApJ, 696, 1029
Churazov, E., Forman, W., Vikhlinin, A., Tremaine, S., Gerhard, O., & Jones, C. 2008, MNRAS, 388, 1062
Clowe, D., Gonzalez, A., & Markevitch, M. 2004, ApJ, 604, 596
Dickey, J. M., & Lockman, F. J. 1990, ARA&A, 28, 215
Finoguenov, A., Böhringer, H., & Zhang, Y.-Y. 2005, A&A, 442, 827
Grevesse, N., & Sauval, A. J. 1998, Space Science Reviews, 85, 161
Gu, L., et al. 2009, ApJ, 700, 1161 (G09)
Guo, F., & Mathews, W. G. 2010, ApJ, 712, 1311
Johnson, R., Chakrabarty, D., O'Sullivan, E., & Raychaudhury, S. 2009, ApJ, 706, 980
Machacek, M., Dosaj, A., Forman, W., Jones, C., Markevitch, M., Vikhlinin, A., Warmflash, A., & Kraft, R. 2005, ApJ, 621, 663
Mahdavi, A., Hoekstra, H., Babul, A., & Henry, J. P. 2008, MNRAS, 384, 1567
Markevitch, M., Vikhlinin, A., & Mazzotta, P. 2001, ApJ, 562, L153
Markevitch, M., Gonzalez, A. H., Clowe, D., Vikhlinin, A., Forman, W., Jones, C., Murray, S., & Tucker, W. 2004, ApJ, 606, 819
McNamara, B. R., & Nulsen, P. E. J. 2007, ARA&A, 45, 117
Nagai, D., Vikhlinin, A., & Kravtsov, A. V. 2007, ApJ, 655, 98
Nulsen, P. E. J., David, L. P., McNamara, B. R., Jones, C., Forman, W. R., & Wise, M. 2002, ApJ, 568, 163

Riemer-Sørensen, S., Paraficz, D., Ferreira, D. D. M., Pedersen, K., Limousin, M., & Dahle, H. 2009, ApJ, 693, 1570
Sand, D. J., Treu, T., Ellis, R. S., Smith, G. P., & Kneib, J.-P. 2008, ApJ, 674, 711
Sanders, J. S. 2006, MNRAS, 371, 829
Sarazin, C. L. 1988, Cambridge Astrophysics Series (Cambridge: Cambridge Univ. Press), 1988
Schuecker, P., Finoguenov, A., Miniati, F., Böhringer, H., & Briel, U. G. 2004, A&A, 426, 387
Shan, H., Qin, B., Fort, B., Tao, C., Wu, X.-P., & Zhao, H. 2010, arXiv:1004.1475
Squires, G., Kaiser, N., Babul, A., Fahlman, G., Woods, D., Neumann, D. M., & Boehringer, H. 1996, ApJ, 461, 572
Vikhlinin, A., Kravtsov, A., Forman, W., Jones, C., Markevitch, M., Murray, S. S., & Van Speybroeck, L. 2006, ApJ, 640, 691
Vikhlinin, A., et al. 2009, ApJ, 692, 1060
Wang, Y., Xu, H., Zhang, Z., Xu, Y., Wu, X.-P., Xue, S.-J., & Li, Z. 2005, ApJ, 631, 197
Wu, X.-P., & Fang, L.-Z. 1996, ApJ, 467, L45
Zhang, Y.-Y., Finoguenov, A., Böhringer, H., Kneib, J.-P., Smith, G. P., Kneissl, R., Okabe, N., & Dahle, H. 2008, A&A, 482, 451
Zhang, Y.-Y., Reiprich, T. H., Finoguenov, A., Hudson, D. S., & Sarazin, C. L. 2009, ApJ, 699, 1178
Zhang, Y.-Y., et al. 2010, ApJ, 711, 1033